ACS APPLIED MATERIALS & INTERFACES

www.acsami.org

Research Article

Origin of Interface Limitation in Zn(O,S)/$CuInS_2$-Based Solar Cells

Mohit Sood,*[,°] Jakob Bombsch,*[,°] Alberto Lomuscio, Sudhanshu Shukla, Claudia Hartmann, Johannes Frisch, Wolfgang Bremsteller, Shigenori Ueda, Regan G. Wilks, Marcus Bär, and Susanne Siebentritt

Cite This: *ACS Appl. Mater. Interfaces* 2022, 14, 9676−9684

Read Online

ACCESS | Metrics & More | Article Recommendations | Supporting Information

ABSTRACT: Copper indium disulfide ($CuInS_2$) grown under Cu-rich conditions exhibits high optical quality but suffers predominantly from charge carrier interface recombination, resulting in poor solar cell performance. An unfavorable "cliff"-like conduction band alignment at the buffer/$CuInS_2$ interface could be a possible cause of enhanced interface recombination in the device. In this work, we exploit direct and inverse photoelectron spectroscopy together with electrical characterization to investigate the cause of interface recombination in chemical bath-deposited Zn(O,S)/co-evaporated $CuInS_2$-based devices. Temperature-dependent current−voltage analyses indeed reveal an activation energy of the dominant charge carrier recombination path, considerably smaller than the absorber bulk band gap, confirming the dominant recombination channel to be present at the Zn(O,S)/$CuInS_2$ interface. However, photoelectron spectroscopy measurements indicate a small (0.1 eV) "spike"-like conduction band offset at the Zn(O,S)/$CuInS_2$ interface, excluding an unfavorable energy-level alignment to be the prominent cause for strong interface recombination. The observed band bending upon interface formation also suggests Fermi-level pinning not to be the main reason, leaving near-interface defects (as recently observed in Cu-rich $CuInSe_2$) as the likely reason for the performance-limiting interface recombination.

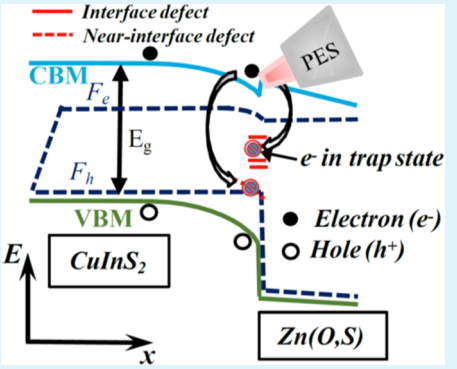

KEYWORDS: *chalcopyrites, thin-film solar cells, $CuInS_2$, direct and inverse photoelectron spectroscopy, energy-level alignment*

INTRODUCTION

Copper indium disulfide ($CuInS_2$), particularly grown under Cu-rich conditions, has been extensively studied in the past and shows superior opto-electronic properties, compared to its Cu-poor counterpart.[1−4] However, the recombination of charge carriers at the buffer/absorber interface remains a bottleneck for devices realized with $CuInS_2$ grown under Cu-rich conditions.[5] This prevents the transfer of the good opto-electronic absorber properties into a high-efficiency solar cell. Specifically, interface recombination remains a major hurdle in achieving high open-circuit voltages (V_{OC}).[6] In devices prepared with a conventional CdS buffer layer, a negative conduction band offset (CBO), that is, a "cliff", in the conduction band at the buffer/absorber (CdS/$CuInS_2$) interface is suggested to be the prominent reason for interface recombination.[7−9] Therefore, alternative buffer layers such as Zn(O,S),[10] Zn(Se,O),[11] and In(OH,S)[12] have been employed in the past. Among these, Zn(O,S) buffer layers remain the most promising candidates, already resulting in devices with a maximum power conversion efficiency (PCE) of 11%.[10] In the previous energy-level alignment study of the Zn(O,S)/$CuInS_2$ interface, we found the presence of a significant positive (i.e., "spike"-like) CBO.[13] However, in this particular case, a ZnS layer was identified to form directly at the buffer/absorber interface.[14] Further, CBO was estimated based on the measured valence band offset (VBO) and the difference in optical (bulk) band gap energies of the absorber and buffer material.[13] However, since the surface band gap of chalcopyrite absorbers strongly differ from their bulk band gap,[15] the actual CBO might vary significantly.

To directly access the electronic structure at the Zn(O,S)/CIS interface and ultimately shed light on the V_{OC} loss of solar cells based on $CuInS_2$ absorbers grown under Cu-rich and Cu-poor conditions, respectively, we use electrical characterization of the respective devices in combination with ultraviolet (UPS), soft X-ray (XPS), and hard X-ray (HAXPES) photoelectron spectroscopy as well as inverse (IPES) photoelectron spectroscopy measurements of the corresponding buffer/absorber interfaces. For this, devices are fabricated with wet-chemically deposited Zn(O,S) buffer layers. The solar cells are analyzed using current−voltage (I−V) and temperature-dependent current−voltage (I−VT) measurements. The measurements reveal the presence of significant charge carrier

Received: October 5, 2021
Accepted: January 11, 2022
Published: February 8, 2022

recombination at the buffer/absorber interface in $CuInS_2$ devices realized with absorbers grown under Cu-rich conditions but not in those based on Cu-poor absorbers. To elucidate the origin of the different recombination pathways, the energy-level alignment at the respective Zn(O,S)/$CuInS_2$ interfaces is explored with particular emphasis on directly probing not only the VBO but also the CBO. For this purpose, thickness series of Zn(O,S) deposited on Cu-rich and Cu-poor $CuInS_2$ absorbers, respectively, are studied using direct and inverse photoemission. We find a small positive "spike"-like CBO at the interface in both cases, excluding an unfavorable CBO as the cause of V_{OC} loss in Cu-rich grown $CuInS_2$-based devices. The observed changes in band bending upon interface formation also suggest Fermi-level pinning not to be the main cause. This is in agreement with our recent finding of significant charge carrier recombination *via* acceptor-like defects in the vicinity of the buffer/absorber interface,[16] leading to a local limitation of the quasi-Fermi-level splitting (qFLs) lowering the overall V_{OC} of the device.

EXPERIMENTAL SECTION

Sample Preparation and Handling. $CuInS_2$ polycrystalline thin films were grown on molybdenum-coated soda-lime glass by the thermal co-evaporation process. In order to prepare $CuInS_2$ films with [Cu]/[In] > 1 (Cu-rich) and [Cu]/[In] < 1 (Cu-poor) as-grown stoichiometry, two different process types were used: a two-stage process to prepare Cu-rich films and a one-stage process to prepare Cu-poor films as explained in detail in ref 4. The Cu-rich absorbers were subjected to a 10% KCN etching for 5 min to remove the $Cu_{2-x}S$ secondary phase, and the Cu-poor films were subjected to a 5% KCN etching for 30 s to ensure reproducible surface conditions.[17,18] Following etching, the absorbers were rinsed with and stored in de-ionized (DI) water until buffer deposition to avoid air exposure. Keeping a DI water film on top to protect the surface during transfer, these films were subsequently dipped in a wet-chemical bath for depositing the Zn(O,S) buffer layer. For preparation of this bath solution, 5.75 g of $ZnSO_4{\cdot}7H_2O$ and 6.09 g of CH_4N_2S were dissolved separately in 60 mL of DI water each and heated at 84 °C for 10 min. After 10 min of preheating, 27 mL of NH_4OH is added to the $ZnSO_4{\cdot}7H_2O$ aqueous solution, followed by addition of the CH_4N_2S solution and 53 mL of water. The final volume of the solution was 200 mL. The $CuInS_2$ absorbers were then dipped in this solution at 84 °C. The entire recipe has been adapted and modified from a process reported by Hubert *et al.*[19] To prepare the Zn(O,S) thickness series, the chemical bath deposition (CBD) was stopped after 0.5, 1, 2, 4, 10, and 20 min, of which the latter deposition time represents the standard duration for buffer layers used in solar cells. After buffer deposition, the samples were rinsed in a 10% NH_4OH aqueous solution and stored in DI water until transfer into a nitrogen-filled glovebox (directly attached to the surface analysis system). To minimize air exposure, the samples were placed into the load lock of the glovebox with a DI water layer on top; during pump down, the samples were freeze-dried. In the glovebox, the samples were mounted on sample holders and then directly transferred into the surface analysis system for XPS measurements. Prior to UPS and IPES characterization, the samples were cleaned using a low-energy (50 eV) Ar^+ treatment for 240 min (bare absorbers) and 40 min (20 min CBD Zn(O,S) buffers), respectively.[20] For transfer to the SPring-8 light source, the samples were double-bagged in the nitrogen atmosphere of the glovebox, with the outer bag containing a desiccant. Prior to the HAXPES measurements, exposure of the samples to ambient conditions for approximately 2 h during mounting and introduction into the measurement system were unavoidable. Due to time constraints, the Cu-poor absorber which underwent a 20 min Zn(O,S) CBD could not be measured at SPring-8, and hence, the respective spectra are missing in this work.

Fabrication and Electrical Characterization of Solar Cells. Solar cells were fabricated using both Cu-rich and Cu-poor $CuInS_2$ absorbers employing a chemical bath-deposited Zn(O,S) buffer layer (20 min deposition time). Following buffer deposition, intrinsic zinc-oxide and aluminum-doped zinc-oxide window layers were deposited using AJA magnetron sputtering units. Finally, nickel-aluminum grids were deposited using Leybold UNIVEX e-beam evaporation units as front contacts. To measure the elemental composition of as-grown absorbers, energy-dispersive X-ray spectroscopy (EDX) at 20 kV was performed using a 20 mm^2 area Oxford Instruments X-Max Silicon Drift Detector (SDD) installed in a Hitachi SU-70 field-emission SEM with a Schottky electron source and with a secondary electron detector.

The optical characterization was carried out by illuminating the sample using a Coherent 660 nm continuous wave diode laser. Calibrated photoluminescence (PL) measurements were used to extract the qFLs of the absorbers. This procedure includes two steps: first, using a commercial calibration lamp, a spectral correction is carried out. In the second step, an Andor CCD camera and a power meter are used to perform an intensity correction. This information is then used to tune the intensity of the laser in order to excite the sample with an intensity equivalent to 1 sun (i.e., the same flux of photons as in an AM1.5 spectrum with energies above the band gap). The qFLs is then extracted from the PL measurements by transforming the PL flux into energy space using Planck's generalized law[21] and fitting the high-energy slope.[22] A detailed description of the process can be found in ref 23.

For electrical characterization of the solar cells, an OAI AAA solar simulator unit with a standard Xenon short-arc lamp (calibrated to 100 mW/cm^2 AM 1.5 using a reference Si solar cell) with a Keithley *I*−*V* source-measure unit was used to measure the *I*−*V* characteristics of the device at room temperature (25 °C). For external quantum efficiency (EQE) measurements, a Bentham EQE system was used, consisting of a halogen lamp and a xenon lamp as light sources together with a grating monochromator, a light chopper, and a lock-in amplifier. To perform low-temperature electrical characterization (*I*−*VT*), a homemade setup was used. The devices were mounted inside a closed-cycle cryostat operated at $<5 \times 10^{-3}$ mbar. A cold mirror halogen lamp adjusted to an intensity of ∼100 mW/cm^2 was used to illuminate the device for *I*−*VT* measurements. The equivalent calibration of the lamp was done by adjusting the lamp to the sample distance and obtaining a short-circuit current (I_{sc}) equal to the one measured under the solar simulator. To ensure accurate determination of the device temperature during characterization, a Si-diode sensor glued onto an identical glass substrate was placed beside the solar cell. For capacitance profiling, the same setup was used together with an inductance, capacitance, and resistance meter for frequencies in the range f = 20 Hz to 2 MHz with a controlled small-signal ac voltage pulse of 30 mV root mean square and a dc bias.

Laboratory-Based Photoelectron Spectroscopy. XPS and UPS measurements were conducted using laboratory excitation sources, that is, non-monochromatized Mg Kα (1253.56 eV, referred to as 1.3 keV in the article, Specs XR 50) and He II (40.8 eV, Prevac UVS 40A2) excitation, respectively. The photoelectrons were detected using a ScientaOmicron Argus CU electron analyzer. The pass energy for the core-level detail spectra measurements was set to 20 eV, resulting in an experimental energy resolution of approximately 0.9 eV for the Mg Kα source. For the He II measurements, the pass energy was set to 4 eV, resulting in an energy resolution of approximately 0.1 eV. The binding energy (BE) of the XPS measurements was calibrated by referencing the Au $4f_{7/2}$ peak of a clean, grounded Au foil to a BE of 84.00 eV. The UPS BE was calibrated by referencing the Fermi edge of a clean, grounded Au foil to a BE of 0.00 eV.

Inverse photoelectron spectroscopy (IPES) was performed in the same chamber, using a Kimball Physics Inc. EGPS-1002E electron gun with a BaO-coated filament and an OmniVac IPES1000 channeltron-based counter. IPES spectra were recorded in the isochromat mode (i.e., using a bandpass filter to measure photons of constant energy, varying the energy of the incident electrons) with

https://doi.org/10.1021/acsami.1c19156
ACS Appl. Mater. Interfaces 2022, 14, 9676−9684

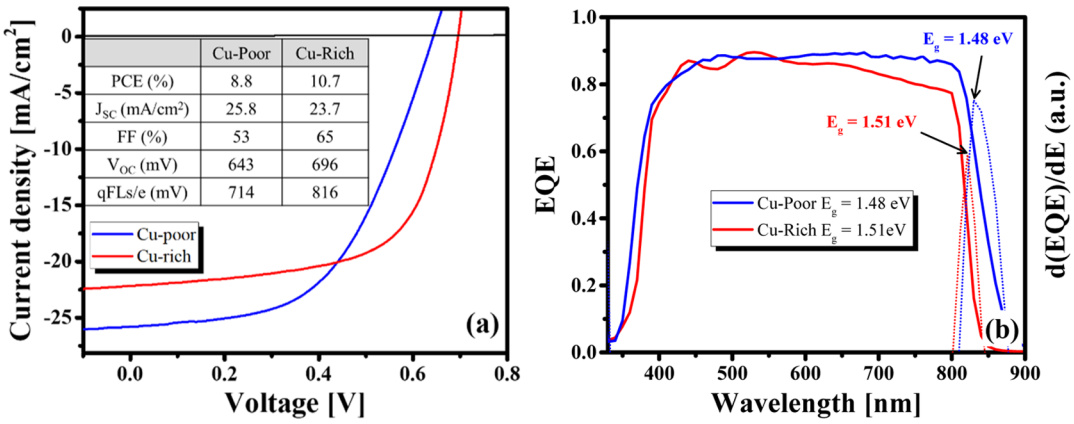

	Cu-Poor	Cu-Rich
PCE (%)	8.8	10.7
J_{SC} (mA/cm²)	25.8	23.7
FF (%)	53	65
V_{OC} (mV)	643	696
qFLs/e (mV)	714	816

Figure 1. (a) Experimentally measured $I-V$ curve of Cu-rich and Cu-poor $CuInS_2$-based devices prepared with the Zn(O,S) buffer layer together with derived device parameters (PCE, J_{SC}, FF, V_{OC}) and the qFLs/e. (b) EQE of Cu-rich (red) and Cu-poor (blue) $CuInS_2$ absorbers with Zn(O,S) layers deposited using CBD with derived $CuInS_2$ band gap energies. The energy derivative of EQE is shown in dots, and the peak energy gives the bulk band gap of the absorber. The legend states the corresponding bulk band gap energies derived from d(EQE)/dE analysis.[27]

the detected photon energy calibrated to 6.69 eV using the Fermi edge of a clean, grounded Au foil. The kinetic energy of the electrons used for excitation was swept from 5 to 15 eV in 0.1 eV steps with a total dwell time (i.e., time per energy at each scan) of 20 s/step. The IPES energy scale was calibrated by referencing the Fermi edge of a clean, grounded Au foil to an energy of 0.0 eV. The energy resolution of the combined electron gun + photon counter IPES system derived from the fit of such a Fermi edge was derived to be approximately 0.9 eV.

The base pressure of the analysis chamber for the XPS (UPS/IPES) measurements was 5×10^{-9} mbar (6×10^{-10} mbar).

Synchrotron-Based Hard X-ray Photoelectron Spectroscopy. HAXPES experiments were conducted at the National Institute for Materials Science (NIMS) contract beamline BL15XU of the Super Photon ring-8 GeV (SPring-8) electron storage ring.[24] The end station is equipped with a Scienta R4000 electron energy analyzer with the following geometrical setup for the beamline and analyzer: horizontally polarized X-rays, with the analyzer entrance lying in the polarization plane. The X-rays hit the sample in grazing incidence, and emitted electrons are detected at an angle close to 90° relative to the sample surface. Spectra were excited using a calibrated photon energy of 5.95 keV (referred to as 6 keV in the article) using the Si(111) crystal of a double-crystal monochromator and a Si(333) channel-cut monochromator. A pass energy of 200 eV was used for all measurements, resulting in a combined analyzer plus X-ray energy resolution of approximately 0.25 eV for all HAXPES spectra. The BE was calibrated by referencing the Fermi edge of a grounded clean Au foil to a BE of 0.00 eV. The base pressure of the setup was $<1 \times 10^{-9}$ mbar.

Curve Fit Analysis. XPS and HAXPES core-level spectra were fitted using linear backgrounds and Voigt profiles, keeping—if more than one species is present—the interspecies distances of one core level constant for all excitation energies and keeping the shape of the Voigt profile identical for identical core levels and excitation energies. To consider spin−orbit coupling, two Voigt profiles with a fixed distance in BE and a fixed intensity ratio according to $\frac{1+2(l+1/2)}{1+2(l-1/2)}$ were used.

RESULTS AND DISCUSSION

Figure 1a shows the measured $I-V$ characteristics of solar cells under AM 1.5 illumination made from Cu-rich and Cu-poor $CuInS_2$ absorbers having an EDX-derived (i.e., bulk) [Cu]/[In] ratio of 1.75 and 0.98, respectively, prior KCN etch. Thus, the seemingly high ratio for the Cu-rich absorber might not represent its true bulk composition as it is influenced by the well-known presence of the $Cu_{2-x}S$ secondary surface phase. The device $I-V$ parameters are reported in the table inset of Figure 1a along with the qFLs of the Cu-rich and Cu-poor $CuInS_2$ absorbers measured by calibrated PL (Figure S1). As observed earlier,[4] the Cu-rich absorbers exhibit higher qFLs compared to their Cu-poor $CuInS_2$ counterparts. Between the two devices, the Cu-rich $CuInS_2$ device exhibits superior FF, V_{OC}, and therefore PCE value (inset in Figure 1a) compared to the Cu-poor counterpart. Although the J_{SC} of the Cu-rich device is significantly lower than that of the Cu-poor devices, the V_{OC} and PCE values obtained are similar to earlier reported device parameters of high-efficiency $CuInS_2$ devices based on Cu-rich and Cu-poor $CuInS_2$ absorbers.[10−12,25] Contrary to $CuInSe_2$ (both with and without Ga), where the Cu-poor devices exhibit a higher PCE than the Cu-rich ones,[26] the Ga-free Cu-poor $CuInS_2$ devices exhibit a lower PCE compared to Cu-rich devices. This is because, unlike $CuInSe_2$, the Cu-rich $CuInS_2$ absorbers possess a higher optoelectronic quality than the Cu-poor absorbers (see the table inset of Figure 1).[4,23] The J_{SC} of the Cu-rich devices is smaller due to a higher bulk band gap of ∼1.51 eV compared to a bulk band gap of ∼1.48 eV of the Cu-poor absorbers (E_g obtained by d(EQE)/dE analysis,[27] see Figure 1b) and a lower EQE in the longer-wavelength region, as seen in Figure 1b. The device seems to suffer from a small space charge region or diffusion length that causes a drop in EQE in the longer-wavelength region.[28,29] This is supported by the fact that the Cu-rich devices discussed here have a relatively high doping concentration of $>1 \times 10^{17}$ cm^{-3}, resulting in a narrow SCR compared to Cu-poor devices, for which we find a lower absorber doping concentration of $\sim 1 \times 10^{16}$ cm^{-3} (see Figure S1c).

Despite the higher V_{OC}, the Cu-rich devices show a higher qFLs/e-V_{OC} difference of 120 mV, whereas for the Cu-poor device, the value is 71 mV. A large difference between qFLs/e and V_{OC} indicates losses at interfaces and contacts.[16] In optimized chalcopyrite solar cells, this difference is less than 10 mV,[30] whereas in devices with non-optimized contacts and windows but without interface recombination, the difference can be 60 mV,[23] close to the difference we observe for the Cu-poor $CuInS_2$-based device here. This suggests that the Cu-poor device might be dominated by charge carrier recombination in the bulk, whereas the Cu-rich device is dominated by the interface, in agreement with the findings of Kim *et al.*[31] This

https://doi.org/10.1021/acsami.1c19156
ACS Appl. Mater. Interfaces 2022, 14, 9676−9684

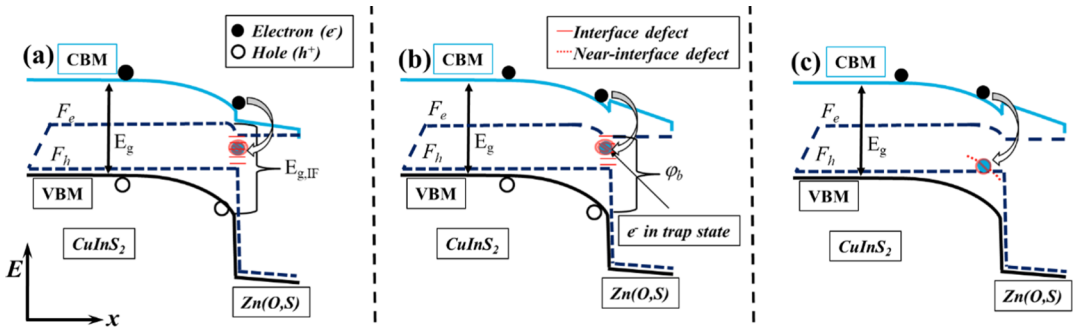

Figure 2. Schematic of the energy-level alignment of the Zn(O,S)/$CuInS_2$ interface under VOC conditions, depicting three possible scenarios: (a) cliff-like CBO and (b) Fermi-level pinning due to interface defects and (c) quasi-Fermi-level gradient due to near-interface defects. Here, F_e and F_h indicate the quasi-Fermi levels for electrons and holes, respectively. All the indicated scenarios cause the activation energy (E_a) of the dominant charge carrier recombination process to be smaller than the absorber bulk band gap (E_g). In (a), E_a equals the interface band gap ($E_{g,IF}$), and in (b), E_a is represented by the hole barrier at the buffer/absorber interface (φ_b). Here, φ_b is nearly voltage-independent in the case of Fermi-level pinning but depends on the voltage in the case of near-interface defects.[16]

fact is further supported by $I-V$ measurements done at different temperatures to reveal the dominant charge carrier recombination mechanism in the devices (see Figure S2). An activation energy (E_a) of 1.34 (±0.02) eV and of 1.44 (±0.05) eV for the dominant charge carrier recombination mechanism in the Cu-rich and Cu-poor $CuInS_2$-based devices, respectively, is obtained by a linear extrapolation of the V_{OC} values to 0 K (see Figure S2c).[32] For the Cu-rich $CuInS_2$-based device, the value of E_a is significantly lower than the bulk band gap (E_g) of $CuInS_2$ (of 1.51 eV obtained by d(EQE)/dE analysis, see Figure S1), in agreement with earlier works.[5,31,33] For the Cu-poor $CuInS_2$ device, E_a agrees (within the experimental uncertainty) with E_g. However, the confidence in E_a is rather low as the device exhibits distortions in its $I-V$ behavior at lower temperatures in an "S shape" (see Figure S2b), which is also the reason why the Cu-poor device has a rather poor FF. Despite this uncertainty, the $I-V$ measurements combined with PL measurements confirm the presence of interface recombination in the Cu-rich $CuInS_2$-based device.

The presence of a negative CBO (i.e., a "cliff") at the buffer/absorber interface or Fermi-level pinning at the interface is the textbook reason for an activation energy $E_a < E_g$ in the device.[34] In the first case, E_a of the dominant recombination path is equal to the interface band gap at the buffer/absorber interface, that is, $E_a = E_{g,IF} = E_g$ + CBO. However, in the second case, E_a of the dominant recombination path is equal to the hole barrier at the buffer/absorber interface, that is, $E_a = \varphi_b$. In addition to these well-known effects, we recently showed that the presence of a significantly high concentration (greater than the doping concentration of the absorber) of deep defects near the CdS/$CuInSe_2$ interface (a so called p+ layer) can also cause a $E_a < E_g$ situation.[16] The qFLs in the vicinity of the interface would be significantly reduced by these deep defect states, thus resulting in a recombination current dominated by the near-interface quasi-Fermi level for electrons. All the three scenarios are depicted in Figure 2.

The energy-level alignment (i.e., whether or not a cliff-like CBO is present) at the buffer/absorber interface can be directly measured by direct and inverse photoemission measurements. Therefore, we address the Zn(O,S)/$CuInS_2$ interface by a combination of UPS, XPS, HAXPES, and IPES measurements.

To examine the energy-level alignment at the buffer/absorber interface, two thickness series of Zn(O,S) were deposited on Cu-rich and Cu-poor $CuInS_2$ absorbers having EDX-derived (bulk) [Cu]/[In] ratios of 1.27 and 0.96, respectively, prior to KCN etch. The thickness series were produced by varying the CBD time and investigated with (photon-energy-dependent) direct and inverse photoelectron spectroscopy. The HAXPES ($h\nu$ = 6 keV) and XPS ($h\nu$ = 1.3 keV, Mg Kα) survey scans (Figures S3 and S4) confirm the presence of all $CuInS_2$-related photoemission and Auger lines, as expected. In addition, peaks ascribed to oxygen and carbon can also be observed, which we attribute to surface adsorbates. On samples with Zn(O,S) buffers, the corresponding Zn, S, and O signals can be seen, increasing in intensity with CBD time, that is, buffer layer thickness. At the same time, the $CuInS_2$ absorber lines decrease in intensity due to attenuation of the photoemission signal by the buffer. Combining Cu 2p with In 3d and Cu 3p with the In 4d core levels derived by XPS and HAXPES, an inelastic mean-free path (IMFP) and therefore the depth-dependent [Cu]/[In] profile of the surface region can be obtained (Figure S5), displaying a similarly Cu-poor surface region for both absorbers with [Cu]/[In] ratios < 0.6 for the upmost surface.

The comparison of absorber-related core-level attenuation derived by XPS and HAXPES indicates that the buffer layer may not cover the (rough) $CuInS_2$ absorber homogeneously, as discussed extensively in the Supporting Information part "Determination of Zn(O,S) thickness". However, no absorber-related signals can be observed for the more surface-sensitive 1.3 keV (Mg Kα) measurements of the 20 min Zn(O,S)/$CuInS_2$ samples (Figures S6 and S7). Thus, it can be concluded that in this case (i.e., for the standard deposition time used to deposit the buffer for solar cells), the buffer layer is continuous and does prevent direct contact between the absorber and window.

As the electronic properties of the buffer strongly depend on the S/O ratio,[35] we study the Zn(O,S) stoichiometry next. The fits of the 6 keV HAXPES Zn 3p spectra of the different samples are displayed in Figure 3. The spectra can only be reasonably fitted using (at least) two contributions: Zn_a and Zn_b, which we tentatively assign to Zn−S and Zn−O bonds, respectively. This assignment is corroborated by the Zn_a contribution having a 1:1 ratio with the ZnS-related S_b component of the S 2p line as discussed in conjunction with Figures S14 and S15. The calculated $Zn_a/(Zn_a + Zn_b)$ ratio directly relates to the "x" of the $ZnO_{1-x}S_x$ composition if a 1:1

https://doi.org/10.1021/acsami.1c19156
ACS Appl. Mater. Interfaces 2022, 14, 9676−9684

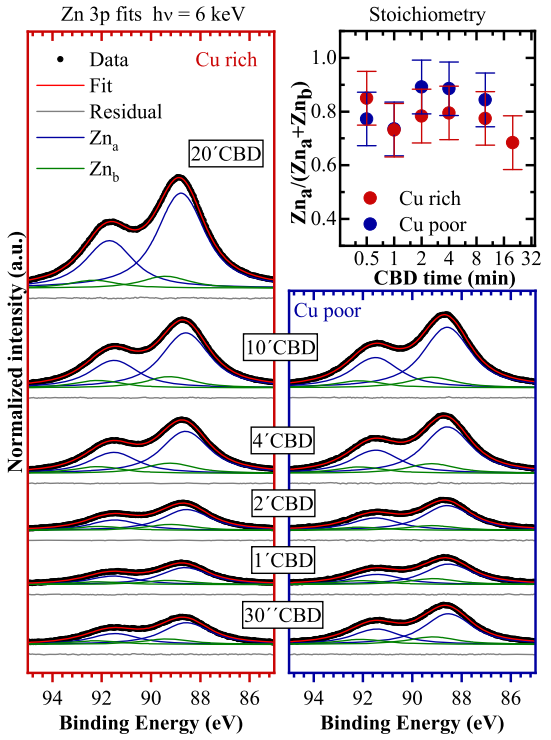

Figure 3. HAXPES (6 keV) spectra of the Zn 3p peak of Cu-rich (left) and Cu-poor (right) $CuInS_2$ samples with the Zn(O,S) buffer layer deposited by different CBD times (from 30 s to 20 min) as indicated. Data are shown with a linear background subtracted. Fits using pairs of Voigt profiles to represent the respective doublets are displayed along the data as well as the respective residuals. The calculated $Zn_a/(Zn_a + Zn_b)$ ratio derived from the displayed fits is shown in the top right panel on a semi-log scale.

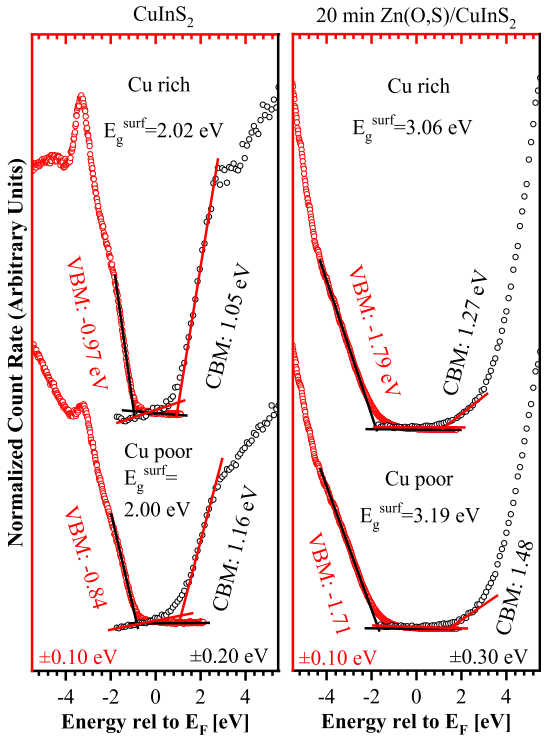

Figure 4. UPS (red) and IPES (black) spectra of Cu-rich (top) and Cu-poor (bottom) $CuInS_2$ absorbers without (a) and with a 20 min CBD Zn(O,S) buffer (b). All samples were treated with 50 eV Ar^+ ions prior to measurements. IPES and UPS spectra are shown on a common energy axis relative to the Fermi level but are displayed on different intensity scales to account for the different backgrounds of both methods. Solid red (IPES) and black (UPS) lines display the linear extrapolation used for determination of the VBM and CBM with respect to the Fermi level (E_F). The VBM and CBM values as well as the derived electronic surface band gap (E_g^{surf} = CBM − VBM) are indicated. The experimental uncertainty of the derived VBM (CBM) values of the $CuInS_2$ absorbers and of the Zn(O,S)/$CuInS_2$ samples is ± 0.1 eV (±0.2 eV for the bare $CuInS_2$ absorber and ± 0.3 eV for the Zn(O,S)/$CuInS_2$ structure), see the text for explanation.

= cation/anion ratio is assumed. The value of x ranges between 0.7 and 0.9 for the Zn(O,S) thickness series and is plotted in the upper right panel of Figure 3. Referencing to previous work on the optical properties of the $ZnO_{1-x}S_x$ systems, an x-value of 0.8, which is in good agreement with our buffer composition, relates to a band gap of approximately 3.1 eV.[35,36]

The UPS and IPES measurements on the Cu-poor and Cu-rich bare $CuInS_2$ absorbers and the respective Zn(O,S) buffers prepared by 20 min CBD give information about the occupied and unoccupied density of states (DOS), respectively. The data sets are shown in Figure 4, together with linear extrapolations of the respective leading edges to determine the position of the band onsets, that is, the valence band maximum (VBM) and conduction band minimum (CBM), with respect to the Fermi level. The extrapolations of the leading edges of all UPS and bare $CuInS_2$ IPES measurements use the clearly dominant edge, as in several previous similar studies.[15,37,38] However, our procedure for estimating the onset of the Zn(O,S) IPES spectra differs and requires more detailed explanation and justification because in this case, we propose that the low-intensity tail of the IPES spectrum, rather than the sharply increasing region of the spectrum, represents the true CBM-related band edge. The explanation for this is based largely on the DOS of the Zn(O,S) conduction band, which depends strongly on the O/S stoichiometry.[35] Considering the respective binaries, calculations indicate that ZnS has a high DOS close to the CBM and thus has a very steep onset, while the onset in ZnO is much more subtle, caused by a largely reduced DOS close to the CBM.[35] Furthermore, it is predicted that the CBM of ZnS is located further away from the Fermi level than that of ZnO. Since even in Zn(O,S), the Zn-anion bond lengths of the binaries are preserved, the bonds are ZnO and ZnS-like also in the alloy.[35] Thus, our measured IPES spectra of the Zn(O,S) buffer represent a superposition of these (low intensity, near the Fermi level) ZnO- and (high intensity, far from the Fermi level) ZnS-derived DOSs; that is, we expect a very shallow (ZnO-related) onset, followed by a very pronounced increase related to a ZnS-like DOS.[35]

Combining the VBM and CBM results, which are also displayed in Figure 4, gives surface band gaps of 2.02 (±0.22) eV and 2.00 (±0.22) eV for the Cu-rich and Cu-poor $CuInS_2$, respectively. These are significantly larger than the respective bulk band gaps of 1.51 and 1.48 eV (see Figure S1d) but are however comparable to previously determined surface band gaps of $CuInS_2$ absorbers.[39] Such a band gap widening toward the surface has also been previously observed for selenide chalcopyrite absorbers[15] and might be related to the observed Cu depletion toward the surface in both absorbers (Figure S4).[39] The band gap widening is expected to be driven by a

https://doi.org/10.1021/acsami.1c19156
ACS Appl. Mater. Interfaces 2022, 14, 9676−9684

VBM shift away from the Fermi level toward the surface, as the p-d repulsion of the Cu 3d- and S 3p-derived states forming the valence band edge is reduced for lower Cu contents.[40] Such a shift can indeed be found in our samples, as can be seen when comparing the less surface-sensitive HAXPES and very surface-sensitive UPS-derived VBM values (Figure S16). However, this shift might—in addition to the band gap widening toward the surface—also in part be caused by a downward band bending toward the surface. More specifically, the difference in UPS-derived VBM values between Cu-poor and Cu-rich absorbers can be assigned to increased surface band bending for the Cu-rich $CuInS_2$, as the derived surface band gaps are very similar in both cases.

The surface band gaps of the Zn(O,S) buffers on the two absorber types are found to be 3.06 (±0.31) eV (Cu-rich $CuInS_2$) and 3.19 (±0.31) eV (Cu-poor $CuInS_2$), in agreement with the 3.1 eV band gap expected based on the [O]/[S] stoichiometry, as discussed above.

The VBM and CBM values of the bare Cu-poor and Cu-rich $CuInS_2$ absorbers and the 20 min Zn(O,S) buffer depicted in Figure 4 already give a coarse (zeroth order) approximation of the interfacial energy-level alignment. In both cases, that is, independent of Cu content of the absorber, we find a negative VBO (i.e., the VBM of the absorber is above that of the buffer) and a positive CBO (i.e., the CBM of the absorber is below that of the buffer) at the buffer/absorber interface. However, the effect of junction formation on the energy levels must also be included in this consideration. This is done by calculating the interface-induced band bending (IIBB).[37] The IIBB can directly be derived from the change of BEs of $CuInS_2$- and Zn(O,S)-related core levels upon buffer deposition. For this, the corresponding XPS data of buffer/absorber samples of the Zn(O,S) thickness series for which both layers could be probed were evaluated. The IIBB was obtained by combining the average of the buffer deposition-induced Cu 2p and In 3d core-level shifts relative to the bare $CuInS_2$ absorber with the shifts of the buffer Zn 2p core level relative to the 20 min CBD Zn(O,S) buffer. The resulting IIBB values for all samples with a buffer layer deposition time of 1 min or longer are displayed in Figure 5 along with the resulting averages of 0.14 eV (Cu-rich $CuInS_2$ interface) and 0.22 eV (Cu-poor $CuInS_2$ interface) and the respective standard deviations of ±0.08 eV (Cu-rich) and ±0.02 eV (Cu-poor). The absolute BE values of all respective core levels can be found in Figures S6 and S7, Tables S1 and S2. As the formation of a p−n junction naturally would lead to a downward band bending in the upper region of the p-type $CuInS_2$ absorber toward the n part of the junction, the observed shift of the Cu 2p and In 3d photoemission lines with increasing buffer layer thickness to a lower BE, displayed in Figure S17, seems to be surprising. However, the shift to a lower absorber core-level BE can also be interpreted as a reduction of the pre-existing downward band bending at the $CuInS_2$ surface due to buffer deposition-induced passivation of charged defects at the surface. Furthermore, the observed shift, particularly on the Cu-rich sample, suggests that Fermi-level pinning is not the main factor that limits V_{OC} and/or causes $E_a < E_g$.

The exact VBO and CBO can then be calculated using IIBB together with the previously determined VBM and CBM values using the following formulae[41]

$$\mathrm{VBO} = \mathrm{VBM_b} - \mathrm{VBM_a} - \mathrm{IIBB} \quad (1)$$

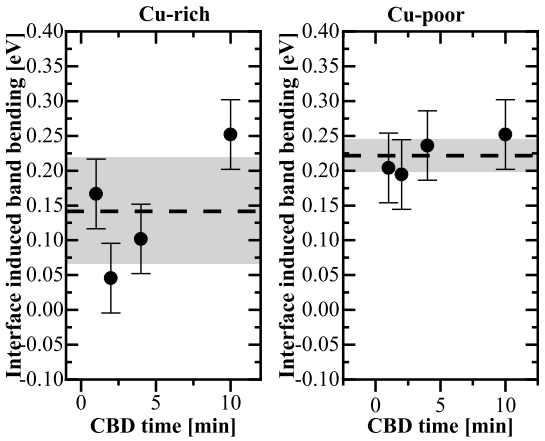

Figure 5. IIBB of the Zn(O,S)/$CuInS_2$ samples using Cu-rich (a) and Cu-poor (b) absorbers. The black dashed lines give the averages of the respective sample, and the gray area visualizes the standard deviation as a measure of confidence. IIBB values were calculated by combining buffer and absorber core-level shifts, which were determined from Cu 2p and In 3d peaks at the absorber side and from Zn 2p for the buffer. All used core-level BEs are given in Tables S1 and S2.

$$\mathrm{CBO} = \mathrm{CBM_b} - \mathrm{CBM_a} - \mathrm{IIBB} \quad (2)$$

where IIBB is the average value depicted as a dashed line in Figure 5 and the subscripts "a" and "b" stand for "absorber" and "buffer", respectively. Including the IIBB, the CBO (VBO) can be determined as +0.08 (±0.36) eV [−0.96 (±0.16) eV] and +0.10 (±0.36) eV [−1.09 (±0.14) eV] for the buffer/absorber interface using the Cu-rich and Cu-poor $CuInS_2$ samples, respectively.

The resulting picture of the energy-level alignment at the Zn(O,S)/$CuInS_2$ interface for the Cu-rich and Cu-poor absorbers is schematically shown in Figure 6. We find a significant cliff-like VBO and a small spike-type offset in the CB at the buffer/absorber interface in both cases, which is the ideal energy-level alignment for this configuration.[42,43] Based on this finding alone, the studied $CuInS_2$-based solar cells should be able to achieve high efficiencies in both the Cu-rich and Cu-poor cases. The positive CBO does not explain the *I*−*VT*-derived $E_a < E_g$ situation, which was suggested to be indicative for the presence of charge carrier recombination at the interface as the dominant (device limiting) mechanism. The observed IIBB further suggests Fermi-level pinning not to be the main cause of an interface-dominated recombination path. This leaves the presence of a near-interface defective layer as a possible explanation for the experimental finding of $E_a < E_g$. Thus, we can conclude that very similar to Cu-rich selenide,[44] the main problem of the Cu-rich sulfide is a defective near-interface layer,[16] likely caused by the necessary etching process.

CONCLUSIONS

We present Cu-rich and Cu-poor $CuInS_2$ absorbers and their solar cells with a Zn(O,S) buffer. As observed previously,[4,31] we find that the performance of the Cu-rich device is limited by interface recombination. We use (direct and inverse) photoelectron spectroscopy on the absorbers and on the absorbers covered successively with the Zn(O,S) buffer to investigate differences between the Cu-rich and Cu-poor absorbers and to determine the energy-level alignment at the

https://doi.org/10.1021/acsami.1c19156
ACS Appl. Mater. Interfaces 2022, 14, 9676−9684

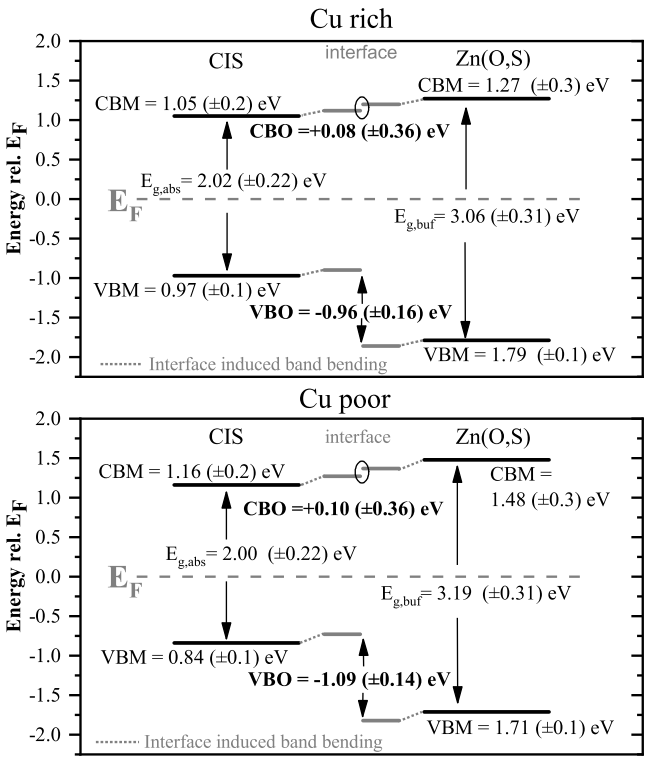

Figure 6. Illustration of the energy-level alignment at the Zn(O,S)/$CuInS_2$ interface when using Cu-rich (top) and Cu-poor (bottom) absorbers. The VBM and CBM values are displayed on the left ($CuInS_2$) and right (Zn(O,S)) side. The VB and CB band offsets considering IIBB are displayed in the center.

buffer/absorber interface. We find that both absorbers have a Cu-deficient surface and exhibit a surface band gap that is larger than the bulk band gap. The CBO between the buffer and absorber in both cases is characterized by a small spike-like offset of about 0.1 eV. This excludes an unfavorable energy-level alignment as the source for the dominating charge carrier interface recombination in the case of Cu-rich absorbers. Furthermore, in both cases, we observe changes in the band bending during interface formation, indicating that Fermi-level pinning is not the main reason for interface recombination as well. This leaves the presence of near-interface defects as the likely reason for the performance limitation of Cu-rich $CuInS_2$-based solar cells, as was recently confirmed for related $CuInSe_2$ absorbers.[16,44]

■ ASSOCIATED CONTENT

Supporting Information

The Supporting Information is available free of charge at https://pubs.acs.org/doi/10.1021/acsami.1c19156.

PL measurements of absorbers, temperature-dependent IV measurements and extended discussion of activation energy and survey and core-level spectra obtained with XPS and HAXPES which are used to determine IMFP-related [Cu]/[In] ratio of absorbers and stoichiometry of the Zn−S phase, detailed discussion of the buffer structure, valence band edge determined from HAXPES, absorber core-level shifts, and a list of the related core-level positions measured with XPS and HAXPES (PDF)

■ AUTHOR INFORMATION

Corresponding Authors

Mohit Sood − *Laboratory for Photovoltaics, Department of Physics and Materials Science, University of Luxembourg, Belvaux L-4422, Luxembourg*; Email: mohit.sood@uni.lu

Jakob Bombsch − *Department Interface Design, Helmholtz-Zentrum Berlin für Materialien und Energie GmbH (HZB), Berlin 12489, Germany*; orcid.org/0000-0002-0820-162X; Email: jakob.bombsch@helmholtz-berlin.de

Authors

Alberto Lomuscio − *Laboratory for Photovoltaics, Department of Physics and Materials Science, University of Luxembourg, Belvaux L-4422, Luxembourg*; orcid.org/0000-0002-3356-2486

Sudhanshu Shukla − *Laboratory for Photovoltaics, Department of Physics and Materials Science, University of Luxembourg, Belvaux L-4422, Luxembourg*

Claudia Hartmann − *Department Interface Design, Helmholtz-Zentrum Berlin für Materialien und Energie GmbH (HZB), Berlin 12489, Germany*

Johannes Frisch − *Department Interface Design, Helmholtz-Zentrum Berlin für Materialien und Energie GmbH (HZB), Berlin 12489, Germany; Energy Materials In situ Laboratory Berlin (EMIL), Helmholtz-Zentrum Berlin für Materialien und Energie GmbH, Berlin 12489, Germany*

Wolfgang Bremsteller − *Department Interface Design, Helmholtz-Zentrum Berlin für Materialien und Energie GmbH (HZB), Berlin 12489, Germany; Energy Materials In situ Laboratory Berlin (EMIL), Helmholtz-Zentrum Berlin für Materialien und Energie GmbH, Berlin 12489, Germany*

Shigenori Ueda − *NIMS Synchrotron X-ray Station at SPring-8, National Institute for Materials Science (NIMS), Sayo, Hyogo 679-5148, Japan; Research Center for Advanced Measurement and Characterization, NIMS, Tsukuba, Ibaraki 305-0047, Japan; Research Center for Functional Materials, NIMS, Tsukuba, Ibaraki 305-0044, Japan*; orcid.org/0000-0001-9425-0614

Regan G. Wilks − *Department Interface Design, Helmholtz-Zentrum Berlin für Materialien und Energie GmbH (HZB), Berlin 12489, Germany; Energy Materials In situ Laboratory Berlin (EMIL), Helmholtz-Zentrum Berlin für Materialien und Energie GmbH, Berlin 12489, Germany*; orcid.org/0000-0001-5822-8399

Marcus Bär − *Department Interface Design, Helmholtz-Zentrum Berlin für Materialien und Energie GmbH (HZB), Berlin 12489, Germany; Energy Materials In situ Laboratory Berlin (EMIL), Helmholtz-Zentrum Berlin für Materialien und Energie GmbH, Berlin 12489, Germany; Department X-ray Spectroscopy at Interfaces of Thin Films, Helmholtz Institute for Renewable Energy (HI ERN), 12489 Berlin, Germany; Department of Chemistry and Pharmacy, Friedrich-Alexander Universität Erlangen-Nürnberg (FAU), 91058 Erlangen, Germany*; orcid.org/0000-0001-8581-0691

Susanne Siebentritt − *Laboratory for Photovoltaics, Department of Physics and Materials Science, University of Luxembourg, Belvaux L-4422, Luxembourg*

Complete contact information is available at: https://pubs.acs.org/10.1021/acsami.1c19156

Author Contributions

°M.S. and J.B. contributions equally.

https://doi.org/10.1021/acsami.1c19156
ACS Appl. Mater. Interfaces 2022, 14, 9676−9684

Notes

The authors declare no competing financial interest.

■ ACKNOWLEDGMENTS

M.S. acknowledges that this research was funded in whole, or in part, by the Luxembourg National Research Fund (FNR) in the framework of the MASSENA project (grant reference [PRIDE 15/10935404]) and the CORRKEST project (grant reference [C15/MS/10386094]). For the purpose of open access, the author has applied for a Creative Commons Attributions 4.0 International (CC BY 4.0) license to any Author Accepted Manuscript version arising from this submission. J.B. acknowledges support from the Graduate School Materials for Solar Energy Conversion (MatSEC) as part of Dahlem Research School. The HAXPES measurements at SPring-8 were performed under an approval of NIMS Synchrotron X-ray Station (Proposal no. 2018A4908) and were supported by the NIMS microstructural characterization platform as a program of "Nanotechnology Platform" (project no. 12024046) of the Ministry of Education, Culture, Sports, Science and Technology (MEXT), Japan.

■ REFERENCES

(1) Siemer, K.; Klaer, J.; Luck, I.; Bruns, J.; Klenk, R.; Bräunig, D. Efficient $CuInS_2$ Solar Cells from a Rapid Thermal Process (RTP). *Sol. Energy Mater. Sol. Cells* **2001**, *67*, 159−166.

(2) Meeder, A.; Schmidt-Weber, P.; Hornauer, U.; Förster, D.; Schubert, T.; Neisser, A.; Merdes, S.; Mainz, R.; Klenk, R. High Voltage $Cu(In,Ga)S_2$ Solar Modules. *Thin Solid Films* **2011**, *519*, 7534−7536.

(3) Lomuscio, A.; Melchiorre, M.; Siebentritt, S. Influence of Stoichiometry and Temperature on Quasi Fermi Level Splitting of Sulfide CIS Absorber Layers. *2018 IEEE 7th World Conference on Photovoltaic Energy Conversion (WCPEC)*; IEEE, 2018; pp 1922−1924.

(4) Lomuscio, A.; Rödel, T.; Schwarz, T.; Gault, B.; Melchiorre, M.; Raabe, D.; Siebentritt, S. Quasi-Fermi-Level Splitting of Cu-Poor and Cu-Rich $CuInS_2$ Absorber Layers. *Prog. Photovoltaics* **2019**, *11*, 054052.

(5) Merdes, S.; Sáez-Araoz, R.; Ennaoui, A.; Klaer, J.; Lux-Steiner, M. C.; Klenk, R. Recombination Mechanisms in Highly Efficient Thin Film $Zn(S,O)/Cu(In,Ga)S_2$ Based Solar Cells. *Appl. Phys. Lett.* **2009**, *95*, 213502.

(6) Kim, S.; Nagai, T.; Tampo, H.; Ishizuka, S.; Shibata, H. Large Open-Circuit Voltage Boosting of Pure Sulfide Chalcopyrite $Cu(In,Ga)S_2$ Prepared Using Cu-Deficient Metal Precursors. *Prog. Photovoltaics* **2020**, *28*, 816.

(7) Hashimoto, Y.; Takeuchi, K.; Ito, K. Band Alignment at $CdS/CuInS_2$ Heterojunction. *Appl. Phys. Lett.* **1995**, *67*, 980−982.

(8) Johnson, B.; Korte, L.; Lußky, T.; Klaer, J.; Lauermann, I. $CuInS_2$−CdS Heterojunction Valence Band Offset Measured with near-UV Constant Final State Yield Spectroscopy. *J. Appl. Phys.* **2009**, *106*, 073712.

(9) Weinhardt, L.; Fuchs, O.; Groß, D.; Storch, G.; Umbach, E.; Dhere, N. G.; Kadam, A. A.; Kulkarni, S. S.; Heske, C. Band Alignment at the $CdS/Cu(In,Ga)S_2$ Interface in Thin-Film Solar Cells. *Appl. Phys. Lett.* **2005**, *86*, 062109.

(10) Ennaoui, A.; Bär, M.; Klaer, J.; Kropp, T.; Sáez-Araoz, R.; Lux-Steiner, M. C. Highly-Efficient Cd-Free $CuInS_2$ Thin-Film Solar Cells and Mini-Modules with Zn(S,O) Buffer Layers Prepared by an Alternative Chemical Bath Process. *Prog. Photovoltaics* **2006**, *14*, 499−511.

(11) Chaparro, A.; Gutierrez, M.; Herrero, J.; Klaer, J. Influence of Chemical Bath Deposition Parameters on the Formation of $CuInS_2$/Zn(Se,O) Junctions for Thin Film Solar Cells. *MRS Online Proc. Libr.* **2001**, *668*, 29.

(12) Braunger, D.; Hariskos, D.; Walter, T.; Schock, H. An 11.4% Efficient Polycrystalline Thin Film Solar Cell Based on $CuInS_2$ with a Cd-Free Buffer Layer. *Sol. Energy Mater. Sol. Cells* **1996**, *40*, 97−102.

(13) Bär, M.; Ennaoui, A.; Klaer, J.; Sáez-Araoz, R.; Kropp, T.; Weinhardt, L.; Heske, C.; Schock, H. W.; Fischer, C. H.; Lux-Steiner, M. C. The Electronic Structure of the $[Zn(S,O)/ZnS]/CuInS_2$ Heterointerface—Impact of Post-Annealing. *Chem. Phys. Lett.* **2006**, *433*, 71−74.

(14) Bär, M.; Ennaoui, A.; Klaer, J.; Kropp, T.; Sáez-Araoz, R.; Allsop, N.; Lauermann, I.; Schock, H.-W.; Lux-Steiner, M. C. Formation of a $ZnS/Zn(S,O)$ Bilayer Buffer on $CuInS_2$ Thin Film Solar Cell Absorbers by Chemical Bath Deposition. *J. Appl. Phys.* **2006**, *99*, 123503.

(15) Bär, M.; Nishiwaki, S.; Weinhardt, L.; Pookpanratana, S.; Fuchs, O.; Blum, M.; Yang, W.; Denlinger, J.; Shafarman, W.; Heske, C. Depth-Resolved Band Gap in $Cu(In,Ga)(S,Se)_2$ Thin Films. *Appl. Phys. Lett.* **2008**, *93*, 244103.

(16) Sood, M.; Urbaniak, A.; Kameni Boumenou, C.; Weiss, T. P.; Elanzeery, H.; Babbe, F.; Werner, F.; Melchiorre, M.; Siebentritt, S. Near Surface Defects: Cause of Deficit between Internal and External Open-Circuit Voltage in Solar Cells. *Prog. Photovoltaics* **2021**, DOI: 10.1002/pip.3483.

(17) Fiechter, S.; Tomm, Y.; Kanis, M.; Scheer, R.; Kautek, W. On the Homogeneity Region, Growth Modes and Optoelectronic Properties of Chalcopyrite-Type $CuInS_2$. *Phys. Status Solidi B* **2008**, *245*, 1761−1771.

(18) Lomuscio, A. *Optical Defect Spectroscopy in $CuInS_2$ Thin Films and Solar Cells*; University of Luxembourg: Esch-sur-Alzette, Luxembourg, 2020.

(19) Hubert, C.; Naghavi, N.; Roussel, O.; Etcheberry, A.; Hariskos, D.; Menner, R.; Powalla, M.; Kerrec, O.; Lincot, D. The Zn(S,O,OH)/ZnMgO Buffer in Thin Film $Cu(In,Ga)(S,Se)_2$-Based Solar Cells Part I: Fast Chemical Bath Deposition of Zn(S,O,OH) Buffer Layers for Industrial Application on Co-Evaporated $Cu(In,Ga)Se_2$ and Electrodeposited $CuIn(S,Se)_2$ Solar Cells. *Prog. Photovoltaics* **2009**, *17*, 470−478.

(20) Weinhardt, L.; Heske, C.; Umbach, E.; Niesen, T. P.; Visbeck, S.; Karg, F. Band Alignment at the I-ZnO/CdS Interface in $Cu(In,Ga)(S,Se)_2$ Thin-Film Solar Cells. *Appl. Phys. Lett.* **2004**, *84*, 3175−3177.

(21) Wurfel, P. The Chemical Potential of Radiation. *J. Phys. C: Solid State Phys.* **1982**, *15*, 3967.

(22) Unold, T.; Gütay, L. Photoluminescence Analysis of Thin-Film Solar Cells. *Adv. Charact. Tech. Thin Film Sol. Cells* **2016**, *1*, 275−297.

(23) Babbe, F.; Choubrac, L.; Siebentritt, S. Quasi Fermi Level Splitting of Cu-Rich and Cu-Poor $Cu(In,Ga)Se_2$ Absorber Layers. *Appl. Phys. Lett.* **2016**, *109*, 082105.

(24) Ueda, S.; Katsuya, Y.; Tanaka, M.; Yoshikawa, H.; Yamashita, Y.; Ishimaru, S.; Matsushita, Y.; Kobayashi, K. Present Status of the NIMS Contract Beamline BL15XU at SPring-8. *AIP Conf. Proc.* **2010**, *1234*, 403−406.

(25) Scheer, R.; Alt, M.; Luck, I.; Lewerenz, H. Electrical Properties of Coevaporated $CuInS_2$ Thin Films. *Sol. Energy Mater. Sol. Cells* **1997**, *49*, 423−430.

(26) Siebentritt, S.; Gütay, L.; Regesch, D.; Aida, Y.; Deprédurand, V. Why Do We Make $Cu(In,Ga)Se_2$ Solar Cells Non-Stoichiometric? *Sol. Energy Mater. Sol. Cells* **2013**, *119*, 18−25.

(27) Carron, R.; Andres, C.; Avancini, E.; Feurer, T.; Nishiwaki, S.; Pisoni, S.; Fu, F.; Lingg, M.; Romanyuk, Y. E.; Buecheler, S.; Tiwari, A. N. Bandgap of Thin Film Solar Cell Absorbers: A Comparison of Various Determination Methods. *Thin Solid Films* **2019**, *669*, 482−486.

(28) Scheer, R.; Schock, H. Thin Film Heterostructures. *Chalcogenide Photovoltaics* **2011**, 9−127.

(29) Gärtner, W. W. Depletion-Layer Photoeffects in Semiconductors. *Phys. Rev.* **1959**, *116*, 84.

(30) Wolter, M. H.; Bissig, B.; Avancini, E.; Carron, R.; Buecheler, S.; Jackson, P.; Siebentritt, S. Influence of Sodium and Rubidium

Postdeposition Treatment on the Quasi-Fermi Level Splitting of $Cu(In,Ga)Se_2$ Thin Films. *IEEE J. Photovolt.* **2018**, *8*, 1320−1325.
(31) Kim, S.; Nagai, T.; Tampo, H.; Ishizuka, S.; Shibata, H. Large Open-Circuit Voltage Boosting of Pure Sulfide Chalcopyrite $Cu(In,Ga)S_2$ Prepared Using Cu-Deficient Metal Precursors. *Prog. Photovoltaics* **2020**, *28*, 816−822.
(32) Nadenau, V.; Rau, U.; Jasenek, A.; Schock, H. W. Electronic Properties of $CuGaSe_2$-Based Heterojunction Solar Cells. Part I. Transport Analysis. *J. Appl. Phys.* **2000**, *87*, 584−593.
(33) Sood, M.; Lomuscio, A.; Werner, F.; Nikolaeva, A.; Dale, P. J.; Melchiorre, M.; Guillot, J.; Abou-Ras, D.; Siebentritt, S. Passivating Surface Defects and Reducing Interface Recombination in $CuInS_2$ Solar Cells by a Facile Solution Treatment. *Sol. RRL.* **2021**, *5*, 2100078.
(34) Scheer, R. Activation Energy of Heterojunction Diode Currents in the Limit of Interface Recombination. *J. Appl. Phys.* **2009**, *105*, 104505.
(35) Persson, C.; Platzer-Björkman, C.; Malmström, J.; Törndahl, T.; Edoff, M. Strong Valence-Band Offset Bowing of $ZnO_{1-x}S_x$ Enhances P-Type Nitrogen Doping of ZnO-Like Alloys. *Phys. Rev. Lett.* **2006**, *97*, 146403.
(36) Grimm, A.; Kieven, D.; Klenk, R.; Lauermann, I.; Neisser, A.; Niesen, T.; Palm, J. Junction Formation in Chalcopyrite Solar Cells by Sputtered Wide Gap Compound Semiconductors. *Thin Solid Films* **2011**, *520*, 1330−1333.
(37) Morkel, M.; Weinhardt, L.; Lohmüller, B.; Heske, C.; Umbach, E.; Riedl, W.; Zweigart, S.; Karg, F. Flat Conduction-Band Alignment at the $CdS/CuInSe_2$ Thin-Film Solar-Cell Heterojunction. *Appl. Phys. Lett.* **2001**, *79*, 4482−4484.
(38) Mezher, M.; Garris, R.; Mansfield, L. M.; Horsley, K.; Weinhardt, L.; Duncan, D. A.; Blum, M.; Rosenberg, S. G.; Bär, M.; Ramanathan, K.; Heske, C. Electronic Structure of the $Zn(O,S)/Cu(In,Ga)Se_2$ Thin-Film Solar Cell Interface. *Prog. Photovoltaics* **2016**, *24*, 1142−1148.
(39) Bär, M.; Klaer, J.; Weinhardt, L.; Wilks, R. G.; Krause, S.; Blum, M.; Yang, W.; Heske, C.; Schock, H. W. $Cu_{2-x}S$ Surface Phases and Their Impact on the Electronic Structure of $CuInS_2$ Thin Films−a Hidden Parameter in Solar Cell Optimization. *Adv. Mater.* **2013**, *3*, 777−781.
(40) Jaffe, J. E.; Zunger, A. Anion Displacements and the Band-Gap Anomaly in Ternary ABC_2 Chalcopyrite Semiconductors. *Phys. Rev. B: Condens. Matter Mater. Phys.* **1983**, *27*, 5176.
(41) Bär, M.; Schubert, B.-A.; Marsen, B.; Wilks, R. G.; Pookpanratana, S.; Blum, M.; Krause, S.; Unold, T.; Yang, W.; Weinhardt, L. Cliff-Like Conduction Band Offset and Kcn-Induced Recombination Barrier Enhancement at the CdS/Cu_2ZnSnS_4 Thin-Film Solar Cell Heterojunction. *Appl. Phys. Lett.* **2011**, *99*, 222105.
(42) Minemoto, T.; Matsui, T.; Takakura, H.; Hamakawa, Y.; Negami, T.; Hashimoto, Y.; Uenoyama, T.; Kitagawa, M. Theoretical Analysis of the Effect of Conduction Band Offset of Window/CIS Layers on Performance of CIS Solar Cells Using Device Simulation. *Sol. Energy Mater. Sol. Cells* **2001**, *67*, 83−88.
(43) Turner, G.; Schwartz, R.; Gray, J. Band Discontinuity and Bulk vs. Interface Recombination in $CdS/CuInSe_2$ Solar Cells. *Conference Record of the Twentieth IEEE Photovoltaic Specialists Conference*; IEEE, 1988; pp 1457−1460.
(44) Elanzeery, H.; Melchiorre, M.; Sood, M.; Babbe, F.; Werner, F.; Brammertz, G.; Siebentritt, S. Challenge in Cu-Rich $CuInSe_2$ Thin Film Solar Cells: Defect Caused by Etching. *Phys. Rev. Mater.* **2019**, *3*, 055403.

https://doi.org/10.1021/acsami.1c19156
ACS Appl. Mater. Interfaces 2022, 14, 9676−9684